THE ASTRONOMICAL JOURNAL, 172:118 (15pp), 2026 August https://doi.org/10.3847/1538-3881/ae7f02

TOI-7169 b: A Hot Jupiter Transiting a Metal-poor Star

Joshua D. Simon[1], Joseph E. Rodriguez[2], Jhon Yana Galarza[3], David W. Latham[4], Victoria DiTomasso[4], Karen A. Collins[4], Jack Schulte[2], Anirudh Chiti[5,29], Samuel N. Quinn[4], Mohammad K. Mardini[6], Shubham Kanodia[7], Johanna K. Teske[1,7], Peter S. Ferguson[8], Samuel W. Yee[9], T. G. Tan[10], Khalid Alsubai[11], Khalid Barkaoui[12,13,14], Zouhair Benkhaldoun[15,16], Krzysztof Bernacki[17], Jaikrit Bhattacharya[18], Jerome P. de Leon[19], Sarah J. Deveny[20,21], Mark E. Everett[22], Izuru Fukuda[23], Akihiko Fukui[19,24], Michaël Gillon[13], Arvind F. Gupta[22], Steve B. Howell[21], Emmanuel Jehin[25], Gaia Lacedelli[24,26], Adam Lark[18], Colin Littlefield[20,21], Felipe Murgas[24,26], Norio Narita[19,24,27], Enric Palle[24,26], Hannu Parviainen[24,26], Adam Popowicz[17], Richard P. Schwarz[4], Avi Shporer[6], Abderahmane Soubkiou[13], and Francis P. Wilkin[28]

[1] Observatories of the Carnegie Institution for Science, 813 Santa Barbara Street, Pasadena, CA 91101, USA; jsimon@carnegiescience.edu
[2] Center for Data Intensive and Time Domain Astronomy, Department of Physics and Astronomy, Michigan State University, East Lansing, MI 48824, USA
[3] Departamento de Astronomía, Universidad de Concepción, Casilla 160-C, Concepción, Chile
[4] Center for Astrophysics | Harvard & Smithsonian, 60 Garden Street, Cambridge, MA 02138, USA
[5] Kavli Institute for Particle Astrophysics & Cosmology, Stanford University, Stanford, CA 94305, USA
[6] Department of Physics and Kavli Institute for Astrophysics and Space Research, Massachusetts Institute of Technology, Cambridge, MA 02139, USA
[7] Earth and Planets Laboratory, Carnegie Institution for Science, 5241 Broad Branch Road Northwest, Washington, DC 20015, USA
[8] DiRAC Institute, Department of Astronomy, University of Washington, 3910 15th Avenue Northeast, Seattle, WA 98195, USA
[9] Department of Physics & Astronomy, University of California Los Angeles, Los Angeles, CA 90095, USA
[10] Perth Exoplanet Survey Telescope, Perth, Western Australia, Australia
[11] Hamad bin Khalifa University (HBKU), Qatar Foundation, P.O. Box 5825, Doha, Qatar
[12] Instituto de Astrofísica de Canarias (IAC), Calle Vía Láctea s/n, E-38200 La Laguna, Tenerife, Spain
[13] Astrobiology Research Unit, Université de Liège, 19C Allée du 6 Août, 4000 Liège, Belgium
[14] Department of Earth, Atmospheric and Planetary Science, Massachusetts Institute of Technology, 77 Massachusetts Avenue, Cambridge, MA 02139, USA
[15] Department of Applied Physics and Astronomy, and Sharjah Academy for Astronomy, Space Sciences and Technology, University of Sharjah, UAE
[16] Cadi Ayyad University, Oukaimeden Observatory, High Energy Physics, Astrophysics and Geoscience Laboratory, FSSM, Morocco
[17] Silesian University of Technology, Akademicka 16, 44-100 Gliwice, Poland
[18] Hamilton College, 198 College Hill Road, Clinton, NY 13413, USA
[19] Komaba Institute for Science, The University of Tokyo, 3-8-1 Komaba, Meguro, Tokyo 153-8902, Japan
[20] Bay Area Environmental Research Institute, Moffett Field, CA 94035, USA
[21] NASA Ames Research Center, Moffett Field, CA 94035, USA
[22] NSF NOIRLab, 950 North Cherry Avenue, Tucson, AZ 85719, USA
[23] Department of Multi-Disciplinary Sciences, Graduate School of Arts and Sciences, The University of Tokyo, 3-8-1 Komaba, Meguro, Tokyo 153-8902, Japan
[24] Instituto de Astrofísica de Canarias (IAC), E-38205 La Laguna, Tenerife, Spain
[25] Space Sciences, Technologies and Astrophysics Research (STAR) Institute, Université de Liège, Allée du 6 Août 19C, B-4000 Liège, Belgium
[26] Departamento de Astrofísica, Universidad de La Laguna (ULL), E-38206 La Laguna, Tenerife, Spain
[27] Astrobiology Center, 2-21-1 Osawa, Mitaka, Tokyo 181-8588, Japan
[28] Department of Physics and Astronomy, Union College, 807 Union Street, Schenectady, NY 12308, USA
Received 2026 March 26; revised 2026 May 31; accepted 2026 June 2; published 2026 July 27

Abstract

Most known planets are found around metal-rich host stars, which has made it difficult to determine whether a lower metallicity limit for planet formation exists and how the properties of planets born in low-metallicity environments may differ from those with metal-rich origins. We present the discovery and characterization of TOI-7169 b (TIC 372048733 b), a hot Jupiter that is orbiting a spectroscopically confirmed metal-poor ([Fe/H] $= -0.72 \pm 0.05$) host star. Based on photometry from TESS and follow-up ground-based imaging, we measure an orbital period of $3.4373125^{+0.0000020}_{-0.0000019}$ days and a planetary radius of $1.475 \pm 0.029\, R_{\rm Jup}$. We use TRES spectroscopy to determine a mass for TOI-7169 b of $0.41 \pm 0.14\, M_{\rm Jup}$. The planet is therefore inflated, with a low density of $0.159^{+0.055}_{-0.054}$ g cm^{-3}. We also characterize the host star, showing that TOI-7169 is ancient (12.3 ± 0.6 Gyr) and α enhanced ([α/Fe] ≈ 0.3), but with a Galactocentric orbit that is confined to the thin disk. TOI-7169 is perhaps the oldest and most metal-poor star currently known to host a transiting giant planet. Future transmission spectroscopy probing the atmosphere of TOI-7169 b may provide insight into the effect of metallicity on the physical properties of giant planets.

Unified Astronomy Thesaurus concepts: Transit photometry (1709); Population II stars (1284); Milky Way disk (1050); Hot Jupiters (753); Exoplanets (498); Exoplanet astronomy (486)

Materials only available in the online version of record: data behind figure

[29] Brinson Prize Fellow

1. Introduction

It is well known that the planet occurrence rate depends on stellar metallicity, in the sense that metal-rich stars are more likely to host planets (e.g., D. A. Fischer & J. Valenti 2005). Based on large samples of planets and extensive surveys of their host stars, recent studies have begun to refine this picture, showing that the occurrence rates of different types of planets and planetary systems may vary in different ways as a function of metallicity (e.g., L. A. Buchhave et al. 2012; A. Mortier et al. 2013; J. M. Brewer et al. 2018; E. A. Petigura et al. 2018; R. Rodríguez Martínez et al. 2023; K. M. Boley et al. 2024; S. Vissapragada & A. Behmard 2025). However, discovery of exoplanets around old and metal-poor stars has remained quite limited, likely because of both lower occurrence rates and the small number of focused searches (e.g., A. Sozzetti et al. 2009; N. C. Santos et al. 2011; A. Mortier et al. 2012; J. P. Faria et al. 2016; D. Barbato et al. 2019; K. M. Boley et al. 2024). The scarcity of known exoplanets with metal-poor host stars hampers our ability to investigate questions such as how planet properties are related to heavy element abundances and what the minimum metallicity required to form planets is.

The NASA Exoplanet Archive list of planets (J. L. Christiansen et al. 2025) includes host stars as metal poor as [Fe/H] $= -2.5$, but the objects at [Fe/H] < -1 all have metallicities determined photometrically rather than spectroscopically. Even at $-1 <$ [Fe/H] < -0.7, the list is dominated by radial velocity (RV) planet detections, Kepler Space Telescope (Kepler) planet candidates that have not been confirmed, companions that are likely in the brown dwarf mass range, stars lacking robust metallicity measurements, and combinations thereof. For planets that were identified by RVs and do not transit, the planetary properties that can be measured are very limited.

Among the sample of metal-poor ([Fe/H] < -0.5) transiting planets, a number of candidates were discovered by the Kepler mission (e.g., T. D. Morton et al. 2016). Most of these are small planets with faint host stars, and nearly all lack reliable metallicities. A notable object in this class is K2-344 b (J. P. de Leon et al. 2021), which is a hot super-Earth around a late K dwarf host with a photometric metallicity of [Fe/H] $= -0.95$. The lowest-metallicity transiting giant planet hosts are WASP-98 at [Fe/H] $= -0.60 \pm 0.19$ (C. Hellier et al. 2014) and WASP-112 at [Fe/H] $= -0.64 \pm 0.15$ (D. R. Anderson et al. 2014). No other transiting giant planets with host stars at [Fe/H] < -0.5 have been confirmed.

Taking advantage of the large number of planet candidates identified by the Transiting Exoplanet Survey Satellite (TESS) and its nearly all-sky coverage (G. R. Ricker et al. 2015), we are conducting a new search aimed at identifying planets orbiting low-metallicity host stars. This effort may help in establishing the lowest metallicity at which the formation of different types of planets is possible, as well as providing better targets for atmospheric characterization of planets that formed in a low-metallicity environment. In this paper, we present the discovery of TOI-7169 b, a giant planet in a short-period orbit around a metal-poor host.

In Section 2, we briefly introduce our search strategy. We present our observations of TOI-7169 in Section 3. In Section 4, we describe our measurements of the properties of the planet and the host star. We discuss the properties of TOI-7169 b in the context of the exoplanet population and the Milky Way in Section 5 and summarize our conclusions in Section 6.

2. Identification of Candidates

The starting point for our search for planets with metal-poor host stars is the catalog of TESS Objects of Interest (TOIs), which currently includes more than 7000 candidate transiting planets. Unlike Kepler, TESS is a magnitude-limited survey that is not biased against metal-poor stars. Some previous studies have used catalogs of metal-poor stars to conduct their own searches for transits in TESS light curves (e.g., K. M. Boley et al. 2021, K. M. Boley et al. 2024). Here, we take the simpler approach of identifying metal-poor stars that already have transits detected by the TESS team.

We select candidate planets that may be hosted by metal-poor ([Fe/H] < -0.5) stars based on several analyses of all-sky, low-resolution spectrophotometric data (i.e., XP spectra; Gaia Collaboration et al. 2023a) from the third data release (DR3) of the Gaia mission (Gaia Collaboration et al. 2016, 2023b). The Gaia team provided a Python tool kit to derive photometry in various passbands from this data product[30] (GaiaXPy 2022). We derive photometry in bands that are known to map onto stellar metallicity, including the SkyMapper filter set (i.e., *v*, *g*, and *i*; S. C. Keller et al. 2007) and a narrowband filter covering the prominent Ca II H and K lines (e.g., E. Starkenburg et al. 2017). Then, we adopt the techniques and model grid described by A. Chiti et al. (2020, 2021) to derive metallicities for stars from this Gaia XP-based photometry via comparison to a grid of synthetic, forward-modeled photometry of stars spanning a range of effective temperatures, surface gravities, and metallicities. The catalog and further details of this analysis will be presented in M. K. Mardini et al. (2026, in preparation). Separately, the Pristine collaboration also released a metallicity catalog of sources in the Gaia XP catalog (N. F. Martin et al. 2024), which we use for our selection as well. We crossmatch both metallicity catalogs with the set of all TOIs to construct an initial candidate sample. This selection is independent of kinematics, so it should include low-metallicity stars regardless of their association with the thin disk, thick disk, or halo of the Milky Way.

For these candidates, we search for spectroscopic metallicities in the GALAH, APOGEE, and LAMOST surveys to confirm their metal-poor nature. Most candidates do not have independent metallicities available, but some can be eliminated in this way. Because the binary fraction of metal-poor stars is high (M. Moe et al. 2019), we next check ExoFOP[31] and the Gaia DR3 catalog (Gaia Collaboration et al. 2023b) for evidence of binarity. We discard targets for which speckle or adaptive optics imaging has revealed a close companion. For stars lacking such high-resolution follow-up imaging, close neighbors in the Gaia stellar catalog, a high reduced unit weight error (RUWE; V. Belokurov et al. 2020; Z. Penoyre et al. 2022; Gaia Collaboration et al. 2023c), or an `ipd_frac_multi_peak` value above two (K. El-Badry et al. 2021; C. Fabricius et al. 2021; Gaia Collaboration et al. 2021) may indicate binarity. Although a binary companion does not necessarily mean that the TESS signal is of nonplanetary origin, it significantly complicates the follow-up, making it challenging to determine which star hosts the transit and potentially biasing precision RV measurements. We therefore set aside binaries for the time being, which eliminates ∼two-thirds of the ∼100 metal-poor candidates. After removing confirmed or likely binaries, stars with spectroscopic metallicities demonstrating that they are not

30 https://gaia-dpci.github.io/GaiaXPy-website/
31 https://exofop.ipac.caltech.edu/tess/

Table 1
TOI-7169 Astrometry and Photometry

Parameter	Value
R.A. (HH:MM:SS.SSSSSS)	23:24:13.126941 ± 0.00009
Decl. (DD:MM:SS.SSSSS)	36:49:03.24207 ± 0.00008
Parallax (mas)	2.207 ± 0.012
$\mu_\alpha \cos\delta$ (mas yr^{-1})	34.280 ± 0.011
μ_δ (mas yr^{-1})	8.358 ± 0.011
BP (mag)	12.717 ± 0.003
G (mag)	12.362 ± 0.003
RP (mag)	11.835 ± 0.004
J (mag)	11.197 ± 0.021
H (mag)	10.873 ± 0.028
K_S (mag)	10.808 ± 0.018
W1 (mag)	10.728 ± 0.023
W2 (mag)	10.765 ± 0.020
W3 (mag)	10.699 ± 0.087
W4 (mag)	9.254 ± 0.526

Note. Astrometry is taken from Gaia DR3 (L. Lindegren et al. 2021). Photometry is from Gaia DR3 (M. Riello et al. 2021), the Two Micron All Sky Survey (2MASS; R. M. Cutri et al. 2003), and AllWISE (R. M. Cutri et al. 2021).

metal poor, and companions larger than ~2 R_{Jup}, we are left with 13 candidates with estimated metallicities $-2 <$ [Fe/H] < -0.5 warranting follow-up observations.

One object that passes this selection process is TOI-7169 (Gaia DR3 1913763798475865344), which has an estimated metallicity of [Fe/H] $= -0.64$. The Gaia astrometry contains no indication of an unresolved companion (RUWE = 0.94 and `ipd_frac_multi_peak` = 0), and the closest neighbor in the Gaia DR3 catalog is 2.″4 away and 6 mag fainter (with a very different parallax and proper motion, indicating that the two stars are not physically associated). However, the Gaia spectroscopy does reveal a relatively large velocity amplitude of 23 km s^{-1}.

TOI-7169 was announced by the TESS collaboration as a TOI on 2024 November 14 (N. M. Guerrero et al. 2021). A transiting signal was detected with the SPOC pipeline in data from Sector 83 with a period of 3.44 days, a planetary radius of 15.0 $R_\oplus$, and a signal-to-noise ratio (S/N) of 26. The basic photometric and astrometric parameters of TOI-7169 are listed in Table 1.

3. Observations

3.1. TESS

TOI-7169 was observed by TESS during its prime mission and the first two extended missions in Sectors 16, 57, 83, and 84. The TESS observations were taken as 1800 s cadence full-frame images in Sector 16 and 200 s full-frame images in Sectors 57 and 84. In Sector 83, TOI-7169 was one of 12,000 stars selected for observations at 120 s cadence. Light curves were produced by the Quick Look Pipeline (C. X. Huang et al. 2020a, 2020b) for Sectors 16, 57, and 84 and the SPOC pipeline (J. M. Jenkins et al. 2016; D. A. Caldwell et al. 2020) for Sector 83. Because the star is fainter than T=10.5, it was not classified as a TOI by the Quick Look Pipeline during the TESS prime mission (N. M. Guerrero et al. 2021). However, the transits are deep enough to be clearly detectable in all sectors, as illustrated below.

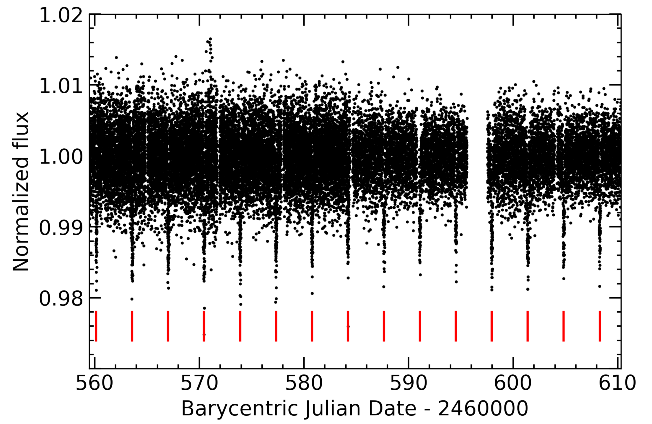

Figure 1. Flattened TESS light curve of TOI-7169 from Sectors 83 (BJD < 2460584.5) and 84 (BJD > 2460584.5). Sector 83 used an integration time of 120 s and the Sector 84 integration time was 200 s. The 15 transits of TOI-7169 b that occur across these two sectors are indicated by red hash marks.

We downloaded the TOI-7169 light curves from the Mikulski Archive for Space Telescopes[32] using the `lightkurve` package (Lightkurve Collaboration et al. 2018). We processed the light curves to remove flux variations from stellar activity and instrumental effects using the spline-fitting tool `keplersplinev2` (A. Vanderburg & J. A. Johnson 2014), following the procedures described by J. Schulte et al. (2024, 2025). The flattened light curve from Sectors 83 and 84 is illustrated in Figure 1.

3.2. Ground-based Photometry

The TESS pixel scale is ~21″ pixel^{-1} and photometric apertures typically extend out to roughly 1′, generally causing multiple stars to blend in the TESS photometric aperture. To determine the true source of the TESS detection and, subsequently, transit depth achromaticity, we acquired ground-based time-series follow-up photometry of the field around TOI-7169 as part of the TESS Follow-up Observing Program (TFOP) Sub Group 1 (SG1; K. Collins 2019).[33] We used the `TESS Transit Finder`, which is a customized version of the `Tapir` software package (E. Jensen 2013), to schedule our transit observations. We used `AstroImageJ` (K. A. Collins et al. 2017) to extract all differential photometric data, except in the case of MuSCAT2 (see below).

As mentioned in Section 2, TIC 2040537885 is a close neighbor of TOI-7169, at a separation of 2.″4 and a magnitude difference of $\Delta G = 6.03$ ($\Delta T = 6.01$). The colors of the two stars are similar, so in an aperture containing both stars, TIC 2040537885 will contribute ≈3.9 ppt of the flux in any optical band. Since the transit depth is 11 ppt (Table 2), TIC 2040537885 cannot be responsible for the transit signal. However, the photometric apertures used for both TESS and all observations discussed below include both stars.

Four partial transits of TOI-7169 were initially observed. The first transit observation was obtained with KeplerCam on UTC 2025 June 22 in Sloan i' band. A second transit was observed with the TRAPPIST-North 0.6 m (K. Barkaoui et al. 2019) telescope in B band on 2025 July 12. The following transit on 2025 July 16 was observed in Sloan g' and Sloan i'

[32] https://mast.stsci.edu/

[33] https://tess.mit.edu/followup

Table 2
Median Values and 68% Confidence Intervals for Transit Times, Impact Parameters, and Depths

Transit	Epoch	T_T (JD)	Depth
TESS UT 2019-09-12 (TESS)	−526	$2458752.12400^{+0.00110}_{-0.00120}$	$0.011104^{+0.000087}_{-0.000089}$
TESS UT 2022-09-30 (TESS)	−201	$2459869.25060^{+0.00054}_{-0.00057}$	$0.011104^{+0.000087}_{-0.000089}$
TESS UT 2024-09-05 (TESS)	3	2460570.46235 ± 0.00021	$0.011104^{+0.000087}_{-0.000089}$
TESS UT 2024-10-01 (TESS)	11	2460597.96085 ± 0.00020	$0.011104^{+0.000087}_{-0.000089}$
MuSCAT2 UT 2025-08-30 (*g*’)	104	2460917.63092 ± 0.00017	$0.011544^{+0.000088}_{-0.000086}$
MuSCAT2 UT 2025-08-30 (*i*’)	104	2460917.63092 ± 0.00017	0.011165 ± 0.000093
MuSCAT2 UT 2025-08-30 (*r*’)	104	2460917.63092 ± 0.00017	$0.011316^{+0.000082}_{-0.000084}$
MuSCAT2 UT 2025-08-30 (*z*’)	104	2460917.63092 ± 0.00017	$0.010965^{+0.000090}_{-0.000091}$
Hamilton UT 2025-09-15 (*r*’)	109	2460934.81748 ± 0.00018	$0.011316^{+0.000082}_{-0.000084}$
LCO-Teid UT 2025-09-29 (*g*’)	113	2460948.56673 ± 0.00018	$0.011544^{+0.000088}_{-0.000086}$
LCO-Teid UT 2025-09-29 (*i*’)	113	2460948.56673 ± 0.00018	0.011165 ± 0.000093

bands from the Las Cumbres Observatory Global Telescope (LCOGT; T. M. Brown et al. 2013) 1.0 m network node at McDonald Observatory near Fort Davis, Texas, United States. The 1.0 m telescopes are equipped with 4096 × 4096 SINISTRO cameras providing a plate scale of 0″389 pixel^{-1} and a field of view of 26′ × 26′. All LCOGT images were calibrated by the standard LCOGT `BANZAI` pipeline (C. McCully et al. 2018). Another transit was observed with the same filters and telescope on 2025 August 23. These data confirmed that the transit is associated with TOI-7169 rather than a nearby star and updated the period slightly to $P = 3.4373111$ days.

The first full transit observation was obtained on 2025 August 29 with the MuSCAT2 multicolor imager (N. Narita et al. 2019) on the 1.52 m Telescopio Carlos Sánchez. MuSCAT2 is capable of simultaneous imaging in four bands, each using a 1000 × 1000 CCD camera with a pixel scale of 0″44 pixel^{-1} and a field of view of 7′4 × 7′4. We used the MuSCAT2 pipeline,[34] described in H. Parviainen et al. (2020), to reduce the data and carry out aperture photometry over a set of comparison stars and aperture sizes. The photometry was contaminated only by TIC 2040537885, but again this object is too faint to be the sourece of the transit signal. The optimal light curves were determined through global optimization of a model consisting of the five brightest comparison stars and contaminated aperture radii smaller than 9″6, while the transit and baseline variations were simultaneously modeled using a linear combination of covariates. As reported in TFOP SG1, we detected an on-time transit with depths in the four bands of $(R_p/R_*)^2 = 9.8,\ 10.5,\ 11.1,$ and 10.0 ppt, which confirms the depth is achromatic within the uncertainties.

A second full transit window of TOI-7169 was observed with a Sloan r' filter on UTC 2025 September 16 from Hamilton College Observatory in Clinton, NY, USA. The 0.51 m telescope is equipped with a QHY600M detector, which has an image scale of 0″45 pixel^{-1}, resulting in a 35′9 × 24′0 field of view. We extracted the differential photometric data with circular photometric apertures having radius 4″05, which excluded the flux from the nearest known neighbor other than TIC 2040537885.

A third full transit of TOI-7169 was observed with the LCOGT 1.0 m network node at Teide Observatory on the island of Tenerife on UT 2025 September 29. The observations were carried out simultaneously in the Sloan i' and Sloan g' filters with exposure times of 28 and 33 s, respectively. We extracted photometry using circular 3″5 photometric apertures.

The full transit observations are listed in Table 2, and light curves from these transits are included in the EXOFASTv2 analysis described in Section 4.2.

3.3. Speckle Imaging

We obtained high-resolution speckle imaging of TOI-7169 with the ’Alopeke instrument (N. J. Scott et al. 2021) on the Gemini-North telescope on 2025 August 6. We observed the star with two narrowband filters, one centered at 562 nm and the other at 832 nm. The data were reduced following the procedures described by S. B. Howell et al. (2011). No nearby sources were detected in either filter. We set lower limits on the magnitude difference of potential companions to TOI-7169 of ∼4.5 mag at a separation of ∼0″1 (Figure 2). At larger separations, the contrast limit reaches ∼6.6 mag in the bluer filter and ∼8.6 mag in the redder filter. Given the observed transit depth, the possibility of the transit actually occurring on a companion star is ruled out for separations between 0″1 and 1″2.

We also observed TOI-7169 with NESSI (N. J. Scott et al. 2018) on the WIYN 3.5 m telescope[35] at Kitt Peak National Observatory. Simultaneous sets of 1000 40 ms diffraction-limited frames were collected on the night of 2025 December 9 in the 562 and 832 nm filters using the blue and red cameras, respectively. The speckle images were reconstructed following the methods outlined in S. B. Howell et al. (2011). We find no evidence for any nearby sources; the achieved 5σ contrast limits are sufficient to rule out resolved sources as faint as $\Delta m_{562} = 4.0$ mag and $\Delta m_{832} = 4.0$ mag at 0″5 and $\Delta m_{562} = 4.2$ mag and $\Delta m_{832} = 4.4$ mag at 1″0.

3.4. Spectroscopy

As part of both our initial vetting of the transit signal and later follow-up to determine the planet mass, we obtained 19 spectra of TOI-7169 with the Tillinghast Reflector Echelle Spectrograph (TRES) on the 1.5 m telescope at Whipple Observatory (A. H. Szentgyorgyi & G. Furész 2007; G. Fűrész 2008). Most of the spectra are concentrated between

[34] https://github.com/hpparvi/MuSCAT2_transit_pipeline

[35] The WIYN Observatory is a joint facility of the University of Wisconsin-Madison, Indiana University, NSF NOIRLab, the Pennsylvania State University, and Princeton University.

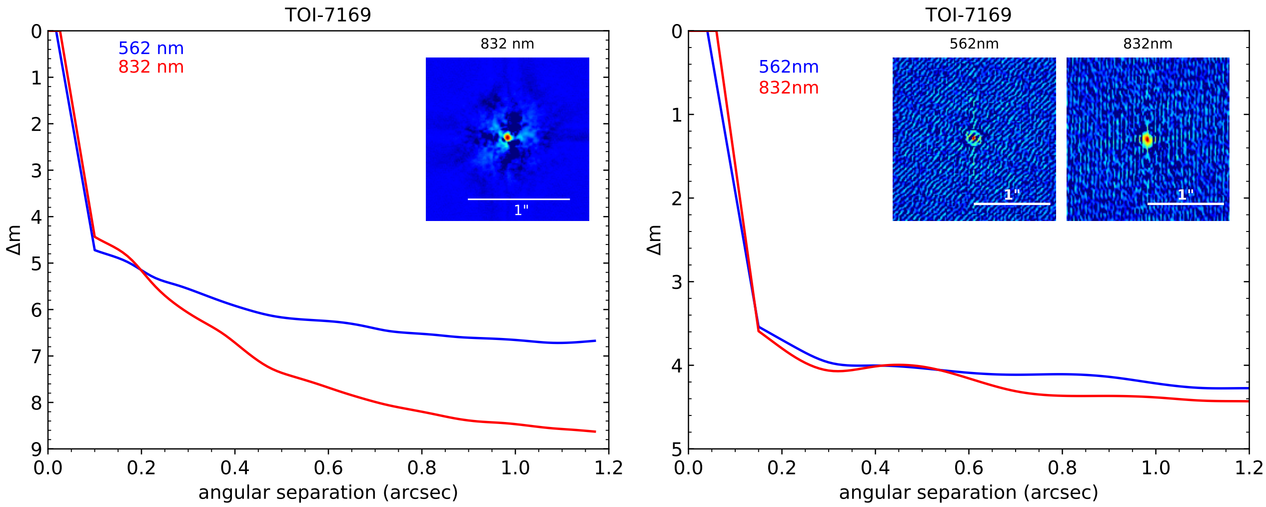

Figure 2. Results from speckle imaging of TOI-7169. Left: Gemini/'Alopeke detection limits. The blue and red curves show the 5σ contrast limits in magnitudes reached in the 562 and 832 nm filters, respectively. The inset in the upper right presents the 832 nm image of the field, with no sources other than the host star detected. Right: WIYN NN-Explore Exoplanet Stellar Speckle Imager (NESSI) 5σ detection limits. The blue and red curves show the contrast limits reached in the 562 and 832 nm filters and the insets show the two reconstructed images.

2024 December 15 and 2025 February 5, but two observations were obtained in 2016 September and two were obtained in 2025 October. TRES provides high-resolution ($R = 44{,}000$) spectra extending from 3850–9100 Å. Data reduction followed the procedures described by L. A. Buchhave et al. (2010) and S. N. Quinn et al. (2012). The S/N of individual spectra was ~30 per resolution element.

We used the TRES spectra to obtain RV measurements of the star's reflex motion resulting from the planetary orbit. The typical velocity precision obtained from each spectrum was ~50 m s^{-1}, which is sufficient for characterizing a giant planet in a short-period orbit. We list the measured RVs in Table 3.

Because of the relatively low S/N of the individual epochs, we coadded the 15 spectra from the end of 2024 and beginning of 2025 together to create a single higher-S/N spectrum for determining the properties of the host star. We used IRAF[36] to apply barycentric and RV corrections with the DOPCOR task. Each spectrum was then normalized in pixel space using the CONTINUUM task with second- to fifth-order polynomials. Finally, the normalized spectra were combined using the SCOMBINE task. The resulting spectrum has an S/N of ~80 at ~630 nm. A small section of the TRES spectrum is displayed in Figure 3, with a TRES solar spectrum (created from the coaddition of all available TRES asteroid spectra by E. K. Pass et al. 2025) overplotted for comparison.

Table 3
TOI-7169 Radial Velocities

BJD	Relative Velocity (m s^{-1})	Velocity Uncertainty (m s^{-1})
2457640.891134	26.3	43.2
2457642.868659	−97.7	39.4
2460660.587476	−228.9	41.3
2460665.729905	36.8	40.1
2460666.719977	10.0	40.4
2460668.675150	−80.1	25.2
2460671.631793	−91.8	39.8
2460675.689780	−61.9	32.9
2460676.728400	−92.5	51.8
2460679.594789	54.2	52.7
2460680.573484	−40.5	40.6
2460681.575481	−156.8	48.5
2460707.592292	−46.5	48.0
2460708.597809	−55.9	61.1
2460710.586763	10.8	34.6
2460711.591263	−11.9	39.0
2460712.606123	−126.9	54.1
2460951.837087	−82.0	41.0
2460976.889632	7.3	58.0

4. Analysis

4.1. Host Star Characterization

We took two independent approaches to measuring the stellar parameters of TOI-7169. First, we used the uberMS framework introduced by E. K. Pass et al. (2025) to fit the order of the TRES data containing the Mg triplet. uberMS employs a neural network to compare the stellar spectrum and photometry with synthetic spectra and theoretical isochrones. The photometric analysis includes fluxes from Gaia (M. Riello et al. 2021), 2MASS (R. M. Cutri et al. 2003), and the Wide-field Infrared Survey Explorer (WISE; E. L. Wright et al. 2010), along with the MIST isochrones (J. Choi et al. 2016). We made two minor modifications to the procedures adopted by E. K. Pass et al. (2025) and V. DiTomasso et al. (2025): (1) we widened the prior on the extinction to encompass from 0 to 1.5× the value from the D. J. Schlegel et al. (1998) dust map, and (2) we added WISE W1 and W2 photometry to better constrain the extinction.

The uberMS fit finds the following parameters for TOI-7169: $T_{\rm eff} = 5840 \pm 100$ K, $\log g = 4.05 \pm 0.09$, $v_{\rm micro} = 1.18$ km s^{-1}, [Fe/H] $= -0.68 \pm 0.04$, and $[\alpha/{\rm Fe}] = 0.22 \pm 0.03$ (V. DiTomasso et al. 2026). The derived distance to the star is 454 pc and the extinction is $A_V = 0.355$ mag, consistent with the Gaia DR3 parallax and the 3D dust map from G. M. Green et al. (2019).

[36] IRAF is distributed by the National Optical Astronomical Observatories, which is operated by the Association of Universities for Research in Astronomy, Inc., under a cooperative agreement with the National Science Foundation.

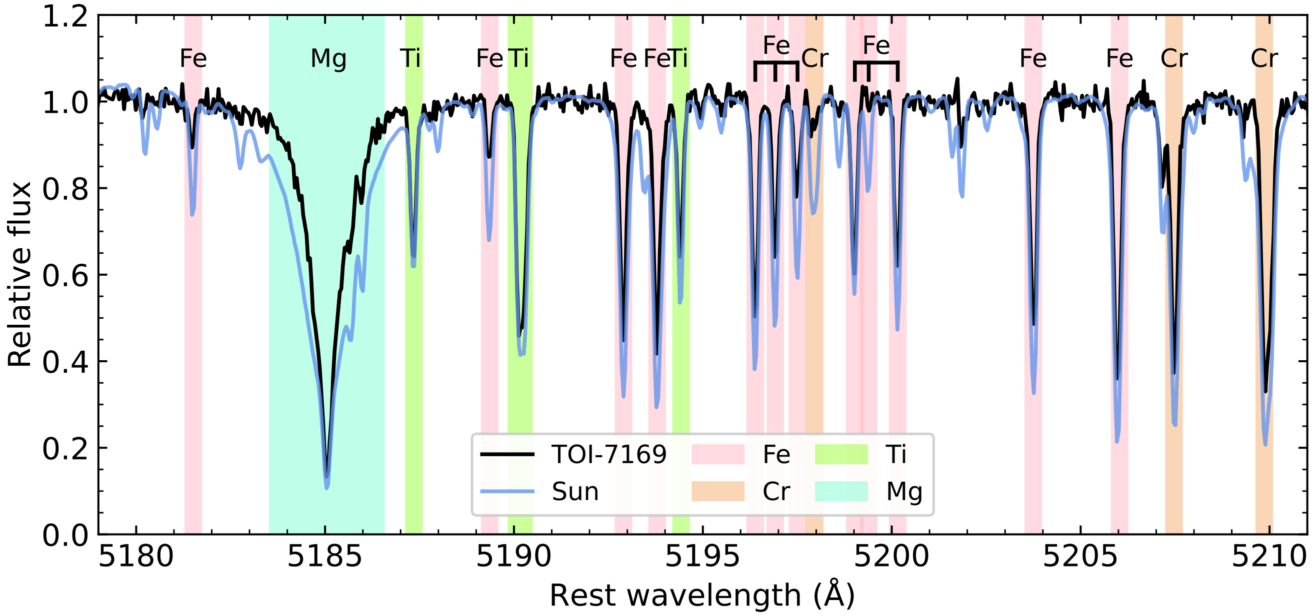

Figure 3. Comparison between the spectrum of TOI-7169 (black) and the Sun (blue). The temperatures of the two stars are quite similar, so the differences in line strength are primarily due to abundance differences (with the exception of the very strong Mg line at 5185 Å). Spectral lines of iron-peak (Fe and Cr) and α elements (Mg and Ti) are shaded as indicated in the legend.

Second, we carried out a traditional equivalent width (EW) analysis (e.g., J. Yana Galarza et al. 2021a, 2024) of the coadded TRES spectrum. We measured EWs by fitting Gaussian profiles with the KAPTEYN `kmpfit` Python package (J. P. Terlouw & M. G. R. Vogelaar 2015), using pseudocontinuum windows of about 6 Å. All measurements were performed manually, line by line, including careful deblending of blended features. We adopted the line list from J. Yana Galarza et al. (2024), which is based on the line list of J. Meléndez et al. (2014) and provided atomic data such as statistical weights and oscillator strengths. We computed the ionization and excitation balance from 62 Fe I lines and 15 Fe II lines using the Qoyllur-quipu (q^2) Python code (I. Ramírez et al. 2014),[37] which is configured to employ the Kurucz ODFNEW model atmospheres (F. Castelli & R. L. Kurucz 2003) and the 2019 version of the local thermodynamic equilibrium (LTE) radiative transfer code MOOG (C. A. Sneden 1973). We adopted the M. Asplund et al. (2021) solar abundances. The EW-based stellar parameters favor a slightly lower temperature than the uberMS fit, but the surface gravity and metallicity are consistent: $T_{\rm eff} = 5714 \pm 42$ K, $\log g = 3.913 \pm 0.130$, $v_{\rm micro} = 1.18 \pm 0.08$ km s^{-1}, and [Fe/H] $= -0.72 \pm 0.05$. The star is a slightly evolved early G star, with a radius of $1.50 \pm 0.03\,R_\odot$. Taking the α-element abundance as an average of [Mg/Fe], [Si/Fe], and [Ca/Fe], we find [α/Fe] $= 0.29 \pm 0.04$. We adopt the stellar parameters from the EW-based analysis for the remainder of the paper (see Table 4).

The stellar age, mass, and radius were also inferred using the q^2 package. Briefly, this Bayesian method adopts the Yonsei–Yale stellar evolution isochrones (S. Yi et al. 2001; P. Demarque et al. 2004) and combines spectroscopically inferred stellar parameters with Gaia magnitudes, parallaxes, and reddening to construct the probability distribution functions for the stellar age, mass, and radius. As the star is enhanced in α elements, we applied an offset to correct their contribution to the global metallicity, following Equation (1) of M. Salaris et al. (1993). Further details are provided in I. Ramírez et al. (2014), J. Yana Galarza et al. (2021b), and G. Martos et al. (2023). We find that the age of TOI-7169 is 12.3 ± 0.6 Gyr (see Figure 4) and the mass is $0.885 \pm 0.010\,M_\odot$. This approach results in small statistical uncertainties because of the high precision of the parallax (2.207 ± 0.012 mas yr^{-1}) and apparent magnitude ($G = 12.362 \pm 0.003$). In general, absolute ages for old stars determined from isochrones are model dependent at the $\sim$1 Gyr level (e.g., T. M. Brown et al. 2014), although in this case we find identical results with the Dartmouth isochrones (A. Dotter et al. 2008) as well. Chemical clocks such as the [Y/Mg] abundance ratio[38] (J. Shejeelammal et al. 2024) provide a consistent age of 14.6 ± 3.4 Gyr, but with significantly lower precision. The derived age is also consistent with the age of 12 Gyr from the thick disk age–metallicity relation of M. Xiang & H.-W. Rix (2022), as shown by J. Adams Redai et al. (2026) for the similar star TOI-7019.

We derived elemental abundances for C I, O I, Na I, Mg I, Al I, Si I, Ca I, Sc I, Sc II, Ti I, Ti II, V I, Cr I, Cr II, Mn I, Fe I, Fe II, Co I, Ni I, Cu I, Zn I, Sr I, Y II, Ba II, Ce II, Nd II, and Sm II. We obtained oxygen abundances from the high-excitation O I 777 nm triplet and corrected for non-LTE

Table 4
Adopted Stellar Parameters of TOI-7169

$T_{\rm eff}$ (K)	$\log g$	[Fe/H]	Age (Gyr)
5714 ± 42	3.913 ± 0.130	−0.72 ± 0.05	12.3 ± 0.6

[37] https://github.com/astroChasqui/q2_tutorial

[38] The calibration from J. Shejeelammal et al. (2024) is only defined down to [Fe/H] $= -0.71$, but given the negligible difference between that value and the derived metallicity of TOI-7169, we assume that no extrapolation is needed.

Table 5
Stellar Abundances

Z	Element	log ϵ	Δ log ϵ	[X/H]	$\sigma_{[X/H]}$	[X/Fe]	$\sigma_{[X/Fe]}$	Number of Lines
6	C I	8.00	0.08	−0.46	0.09	0.26	0.10	2
8	O I	8.05	0.13	−0.64	0.13	0.08	0.14	3
11	Na I	5.66	0.06	−0.56	0.06	0.16	0.08	2
12	Mg I	7.20	0.05	−0.35	0.06	0.37	0.08	5
13	Al I	5.84	0.20	−0.59	0.20	0.13	0.21	2
14	Si I	7.07	0.02	−0.44	0.04	0.28	0.06	11
20	Ca I	5.82	0.04	−0.48	0.05	0.24	0.07	9
21	Sc[a]	2.47	0.06	−0.67	0.07	0.05	0.09	14
22	Ti[a]	4.53	0.04	−0.45	0.06	0.27	0.08	22
23	V I	3.52	0.05	−0.38	0.09	0.34	0.11	5
24	Cr[a]	4.93	0.05	−0.69	0.06	0.03	0.08	11
25	Mn I	4.36	0.04	−1.06	0.07	−0.34	0.09	5
26	Fe[a]	6.74	0.03	−0.72	0.05	...	...	77
27	Co I	4.31	0.08	−0.63	0.09	0.09	0.10	4
28	Ni I	5.57	0.05	−0.63	0.06	0.09	0.08	11
29	Cu I	3.48	0.14	−0.70	0.15	0.02	0.16	2
30	Zn I	4.09	0.08	−0.47	0.09	0.25	0.10	2
38	Sr I	2.13	0.08	−0.70	0.10	0.02	0.11	2
39	Y II	1.41	0.06	−0.80	0.08	−0.08	0.09	4
40	Zr II	2.02	0.10	−0.57	0.10	0.15	0.11	2
56	Ba II	1.38	0.07	−0.89	0.09	−0.17	0.10	3
58	Ce II	1.20	0.10	−0.38	0.10	0.34	0.11	3
60	Nd II	1.07	0.17	−0.35	0.17	0.37	0.18	2
62	Sm II	0.72	0.07	−0.23	0.08	0.49	0.09	3

Note.
[a] Weighted average of the neutral and ionized species.

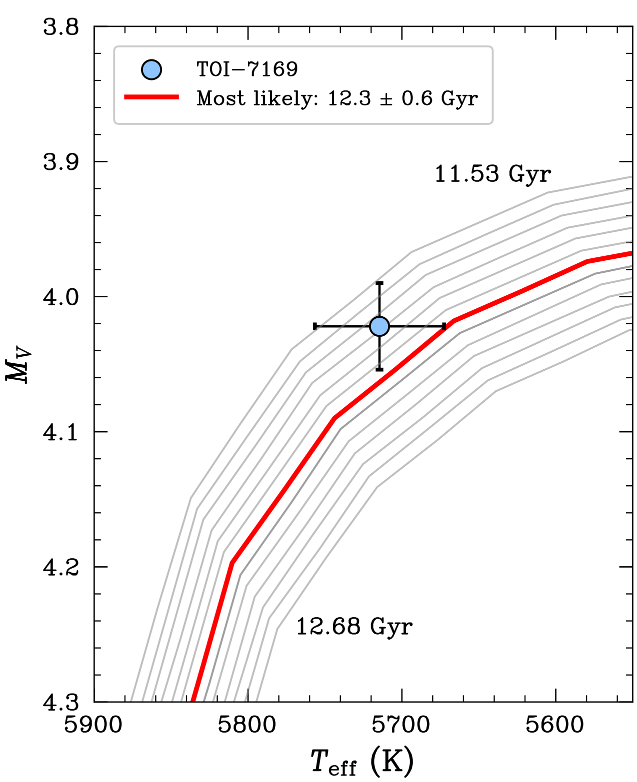

Figure 4. Derived absolute magnitude and effective temperature of TOI-7169 from the q^2 package, compared to Yonsei–Yale isochrones. The red isochrone represents the best-fitting age, which does not exactly match the derived stellar properties because it is a marginalized Bayesian posterior in a higher-dimensional parameter space. The tight constraints on both parameters, and hence on the age, are consequences of the small error bars on the stellar parallax and G-band magnitude from Gaia.

effects using the grids of A. M. Amarsi et al. (2015). All abundances were estimated from EW measurements, following the same procedure used for Fe I and Fe II. We accounted for hyperfine structure and isotopic splitting for Sc I, Sc II, V I, Mn I, Co I, Cu I, Y II, Ba II, and Eu II, adopting data from A. McWilliam (1998), J. X. Prochaska & A. McWilliam (2000), J. X. Prochaska et al. (2000), J. Z. Klose et al. (2002), J. G. Cohen et al. (2003), R. J. Blackwell-Whitehead et al. (2005a, 2005b), J. E. Lawler et al. (2014), and from the Kurucz[39] line lists.

The elemental abundances of TOI-7169 are listed in Table 5 and displayed in Figure 5 along with a comparison sample of stars with broadly similar stellar parameters from the GALAH survey (S. Buder et al. 2025). The GALAH stars are almost all at higher metallicities, but the TOI-7169 abundances are mostly near the values expected if the GALAH abundance trends were extrapolated to [Fe/H] = -0.72. The most notable exception is oxygen, where TOI-7169 has an abundance consistent with solar and typical metal-poor stars have [O/Fe] $>$ 0.5. GALAH and our study measure oxygen from the same features and both apply NLTE corrections, so any systematic offsets should be small. The low oxygen abundance of TOI-7169 is in contrast to its elevated ratios of the other α elements (e.g., Mg, Si, and Ca). The star is also mildly enriched in carbon ([C/Fe] = 0.26) and moderately enriched in the neutron-capture elements past the second r-process peak; lighter neutron-capture species are not enhanced. The combination of a low oxygen abundance and higher carbon abundance produces a slightly supersolar value of [C/O] = 0.18. The corresponding carbon to oxygen ratio is $n_{\rm C}/n_{\rm O}$ = 0.89. This abundance pattern is typical for stars of

[39] http://kurucz.harvard.edu/linelists.html

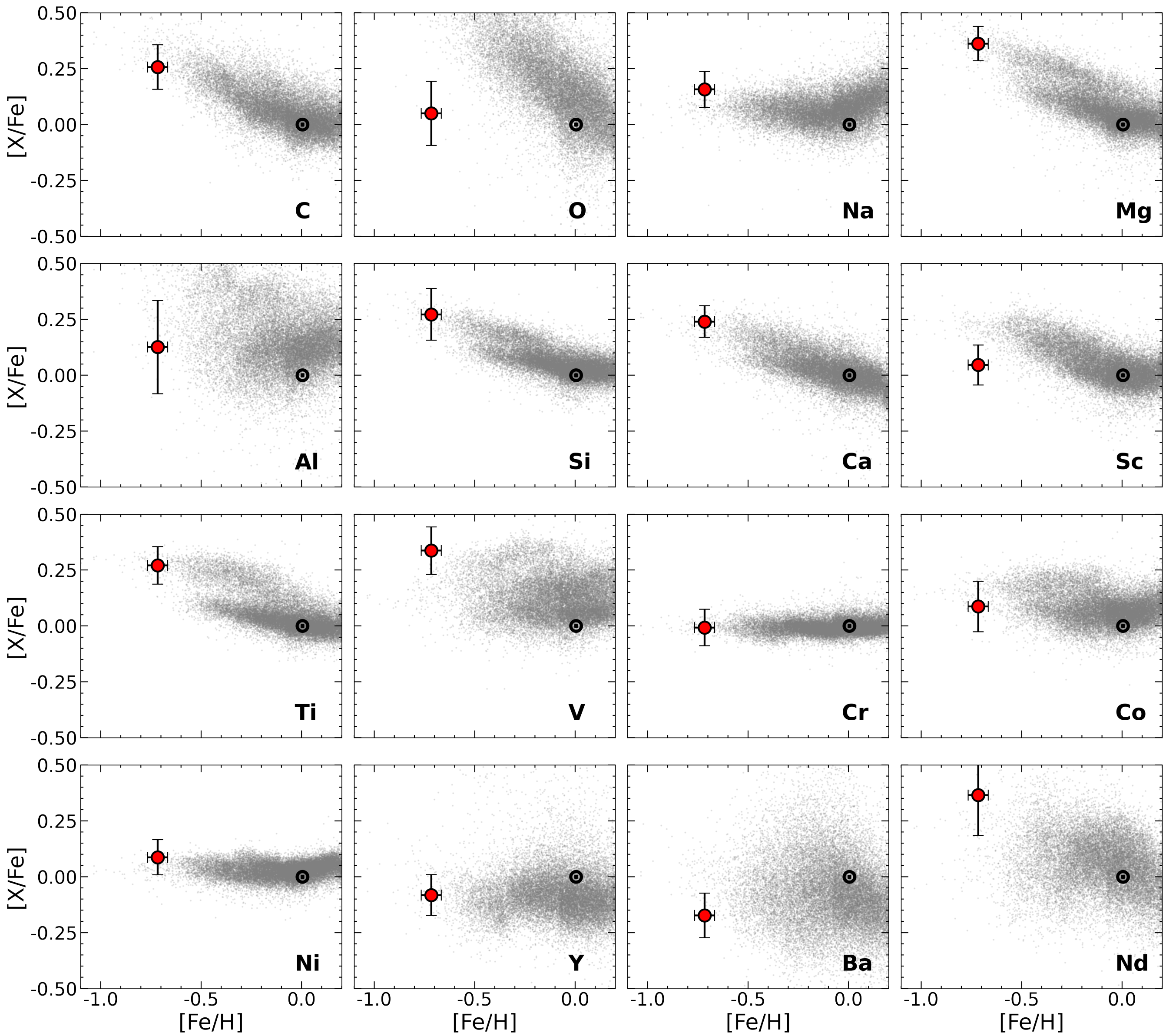

Figure 5. Abundance pattern of TOI-7169. Each of the 16 panels shows the abundance ratio of one element with respect to iron, plotted against metallicity. In each panel, the derived abundance for TOI-7169 is displayed as a red circle, the solar abundance is indicated by the black Sun symbol, and abundances of main-sequence stars from GALAH Data Release 4 (S. Buder et al. 2025) are shown as small gray dots. The TOI-7169 abundances generally agree with the extrapolated trends from GALAH, with the exception of oxygen, which has a significantly lower abundance than expected for a star of its metallicity.

similar age and metallicity, but TOI-7169 has a higher C/O ratio than most planet-hosting stars (e.g., N. R. Hinkel et al. 2014; Y. V. Pavlenko et al. 2019; E. Delgado Mena et al. 2021). Because carbon and oxygen are two of the primary molecule-forming species in planetary atmospheres, their abundance ratio may have an observable impact on atmospheric chemistry and planet properties (e.g., N. Madhusudhan et al. 2011; M. Ali-Dib et al. 2014; C. Helling et al. 2017).

4.2. Derivation of Planetary Properties

We carried out a combined fit of the TESS light curve, ground-based photometry sequences, and TRES RV measurements using EXOFASTv2 (J. Eastman et al. 2013; J. D. Eastman et al. 2019), following the general approach of J. E. Rodriguez et al. (2021) and J. Schulte et al. (2024). Because EXOFASTv2 does not use α-enhanced isochrones that would be appropriate for TOI-7169, we did not include stellar modeling in the fit, but imposed the 1σ parameter ranges for the stellar mass, radius, temperature, metallicity, and age from the spectroscopic analysis (Section 4.1) as Gaussian priors. The EXOFASTv2 fit results are listed in Table 6 and compared to the observed transit light curves and RV measurements in Figure 6.

From the transit depth and the stellar radius, we measure a planetary radius of $1.475 \pm 0.029\,R_{\rm Jup}$. Based on the TRES RVs, the RV semiamplitude of TOI-7169 is 60 ± 20 m s^{-1}, and the orbit is consistent with being circular. (We also ran the EXOFAST fit with the eccentricity held fixed at zero, finding that all fit parameters agree with the free-eccentricity fit within the uncertainties.) The planet mass is $0.41 \pm 0.14\,M_{\rm Jup}$, making TOI-7169 b an inflated Jovian planet with a density of $0.159^{+0.055}_{-0.054}$ g cm^{-3}. The time baseline of the TRES spectra spans ∼9 yr, providing significant sensitivity to long-period stellar or substellar companions. We carried out an initial EXOFAST fit allowing for a linear trend in the RVs, which produced a best fit consistent with no trend (as is visually evident from the data in Figure 6 and Table 3). The final fit described above was therefore run with the trend fixed to zero.

5. Discussion

5.1. Comparison to Exoplanet Population and Occurrence Rates

As discussed in Section 1, confirmed planets have been identified down to metallicities of [Fe/H] ≈ −0.7, with some candidate planets at [Fe/H] = −0.8, −0.9, and below. The best candidates for genuine exoplanets in this metallicity range include Kapteyn's Star b and c at [Fe/H] = −0.89 (G. Anglada-Escude et al. 2014; although see A. Bortle et al. 2021), HD 11755 b at [Fe/H] = −0.74 (B. C. Lee et al. 2015), BD+03 2562 at [Fe/H] = −0.71 (E. Villaver et al. 2017), and 24 Boo b at [Fe/H] ≈ −0.7 (T. Takarada et al. 2018). However, none of these planets transit their host stars, so their composition and atmospheres are not observable. In this metallicity range, the transiting sample consists primarily of small planet candidates, with host star metallicities that have not been spectroscopically confirmed. The only transiting giant planets in the literature at [Fe/H] < −0.5 are WASP-98 b ([Fe/H] = −0.60: C. Hellier et al. 2014; [Fe/H] = −0.49 ± 0.10: L. Mancini et al. 2016) and WASP-112 b ([Fe/H] = −0.64: D. R. Anderson et al. 2014; [Fe/H] = −0.54 ± 0.05: T. Ferreira et al. 2025). TOI-7169 is therefore likely the most metal-poor host of a transiting giant planet currently known.

K. M. Boley et al. (2021) determined an upper limit on the occurrence rate of short-period giant planets of 0.18% for stars at [Fe/H] < −0.6. This result suggests that a sample of $\gtrsim$550 metal-poor stars would need to be searched in order to find a planet like TOI-7169 b. From Table 6, the transit probability for TOI-7169 b is 0.18, which increases the required search sample to $\gtrsim$3100 metal-poor stars. The Gaia DR3 catalog contains ∼360,000 stars with $G < 12.5$ and spectrophotometric metallicities [M/H] < −0.6. Presuming that TESS has observed most of these stars, the K. M. Boley et al. (2021) limit indicates that up to ∼100 similar planets could be detectable.

In addition to their variation with metallicity, J. K. Zink et al. (2023) found that planet occurrence rates are also a function of Galactic oscillation height (the maximum distance away from the Galactic plane that a star's orbit reaches), in the sense that stars found farther above or below the plane are less likely to host planets. There is not yet any consensus on the origin of this correlation, but suggestions include an increase in the formation rate of systems with tightly packed inner planets with time (S. Ballard 2024), decreased accretion rates from the interstellar medium for protoplanetary disks outside the Galactic midplane (A. J. Winter et al. 2024), and the intense ultraviolet radiation fields experienced by disks that formed $\gtrsim$10 Gyr ago when the local star formation rate was much higher (T. Hallatt & E. J. Lee 2025). As shown in Section 5.3, despite its low metallicity, TOI-7169 has a maximum z-height of 200 pc, whereas J. K. Zink et al. (2023) did not detect a measurable decrease in occurrence rates until $z \gtrsim 500$ pc. If the J. K. Zink et al. (2023) measurements apply to giant planets (their sample was only statistically significant for small planets), then TOI-7169 b may fit in with the idea that stars closer to the Galactic plane are more likely to host planets, independent of their metallicities.

Table 6
Median Values and 68% Confidence Intervals for TOI-7169 b, Created using EXOFASTv2 Commit Number 6ba004d4

Parameter	Description	Values
Planetary Parameters		
P	Period (days)	$3.4373125^{+0.0000020}_{-0.0000019}$
R_p	Radius ($R_{\rm Jup}$)	1.475 ± 0.029
M_p	Mass ($M_{\rm Jup}$)	0.41 ± 0.14
T_c	Observed time of conjunction[a] (BJD$_{\rm TDB}$)	$2460560.15083^{+0.00061}_{-0.00040}$
a	Semimajor axis (au)	$0.04280^{+0.00016}_{-0.00017}$
i	Inclination (deg)	84.62 ± 0.26
e	Eccentricity	$0.055^{+0.110}_{-0.041}$
ω_*	Argument of periastron (deg)	-6^{+71}_{-110}
T_{eq}	Equilibrium temperature[b] (K)	1631^{+19}_{-20}
$\tau_{\rm circ}$	Tidal circularization timescale (Gyr)	$0.030^{+0.013}_{-0.012}$
K	RV semiamplitude (m s^{-1})	60 ± 20
R_p/R_*	Radius of planet in stellar radii	0.10116 ± 0.00054
a/R_*	Semimajor axis in stellar radii	$6.14^{+0.12}_{-0.11}$
δ	$(R_p/R_*)^2$	0.01023 ± 0.00011
τ	Ingress–egress transit duration (days)	$0.02237^{+0.00093}_{-0.00092}$
T_{14}	Total transit duration (days)	$0.16882^{+0.00085}_{-0.00084}$
b	Transit impact parameter	$0.573^{+0.021}_{-0.023}$
b_s	Eclipse impact parameter	$0.567^{+0.024}_{-0.026}$
$T_{s,14}$	Total eclipse duration (days)	$0.1681^{+0.0043}_{-0.0054}$
$\delta_{s,2.5\,\mu m}$	BB eclipse depth at 2.5 μm (ppm)	537 ± 21
$\delta_{s,5.0\,\mu m}$	BB eclipse depth at 5.0 μm (ppm)	1382^{+34}_{-35}
$\delta_{s,7.5\,\mu m}$	BB eclipse depth at 7.5 μm (ppm)	1817^{+37}_{-38}
ρ_p	Density (g cm^{-3})	$0.159^{+0.055}_{-0.054}$
$\log g_p$	Surface gravity (cgs)	$2.67^{+0.13}_{-0.18}$
$\langle F \rangle$	Incident flux (10^9 erg s^{-1} cm^{-2})	$1.591^{+0.080}_{-0.083}$
T_s	Observed time of eclipse (BJD$_{\rm TDB}$)	$2460558.48^{+0.28}_{-0.10}$
T_p	Time of periastron (TJD$_{\rm TDB}$)	$2460559.46^{+1.20}_{-0.51}$
M_p/M_*	Mass ratio	0.00044 ± 0.00015
$P_{T,G}$	A priori transit probability	$0.1801^{+0.0077}_{-0.0063}$
Wavelength Parameters		
$u_1(g')$	Linear limb-darkening coefficient	0.484 ± 0.028
$u_1(r')$	Linear limb-darkening coefficient	0.263 ± 0.031
$u_1(i')$	Linear limb-darkening coefficient	0.337 ± 0.028
$u_1(z')$	Linear limb-darkening coefficient	0.177 ± 0.039
u_1(TESS)	Linear limb-darkening coefficient	0.250 ± 0.023
$u_2(g')$	Quadratic limb-darkening coefficient	0.232 ± 0.031
$u_2(r')$	Quadratic limb-darkening coefficient	$0.299^{+0.033}_{-0.032}$
$u_2(i')$	Quadratic limb-darkening coefficient	0.294 ± 0.031
$u_2(z')$	Quadratic limb-darkening coefficient	$0.283^{+0.044}_{-0.043}$
u_2(TESS)	Quadratic limb-darkening coefficient	$0.280^{+0.024}_{-0.023}$
Telescope Parameters		TRES
$\gamma_{\rm rel}$	Relative RV offset (m s^{-1})	-57^{+15}_{-14}
σ_J	RV jitter (m s^{-1})	43^{+18}_{-16}

Notes. See Table 3 in J. D. Eastman et al. (2019) for a detailed description of all parameters.
[a] Time of conjunction is commonly reported as the "transit time."
[b] Assumes no albedo and perfect redistribution.

5.2. Is a Low Host Star Metallicity Associated with Low Planet Density?

Given the low density of TOI-7169 b, it is tempting to conclude that a low host star metallicity is related to the formation of less dense planets. Other giant planets around

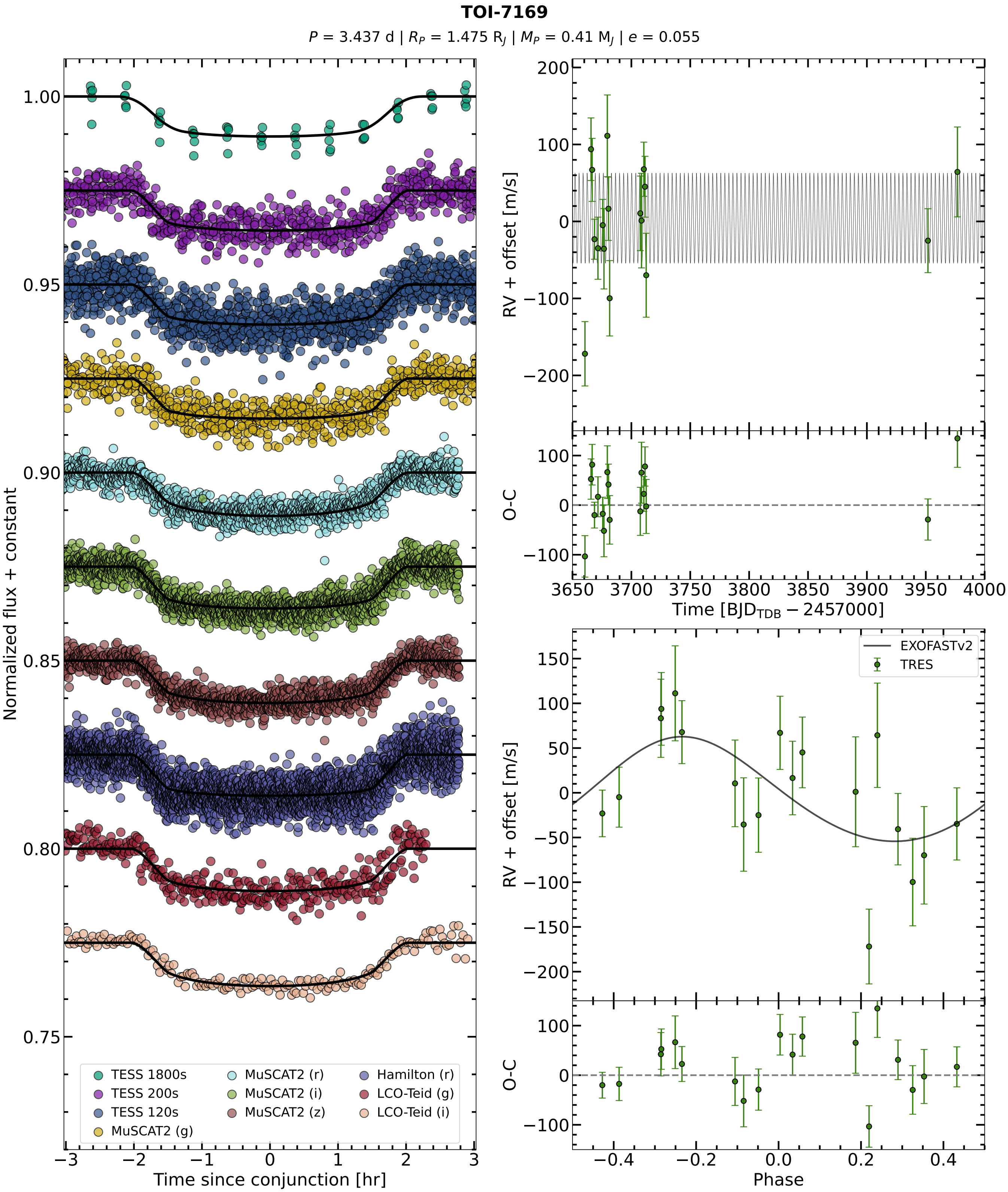

Figure 6. EXOFASTv2 fit results for TOI-7169. The left panel displays the stacked TESS transits and the full transits observed from the ground along with the best-fit model of each. The panel in the upper right plots the TRES RVs and the best-fit orbit model, with residuals below. Note that the two velocity measurements from 2016 are not plotted in the upper right panel so that the bulk of the data remain visible. The panel in the lower right shows the phase-folded RVs.

(The data used to create this figure are available in the online article.)

metal-poor stars, such as WASP-98 b (C. Hellier et al. 2014) and WASP-112 b (D. R. Anderson et al. 2014), also have densities substantially lower than that of Jupiter, supporting this idea. In addition, A. Behmard et al. (2025) showed that for rocky planets, there is a significant anticorrelation between density and [Mg/Fe]. The low density and high Mg abundance

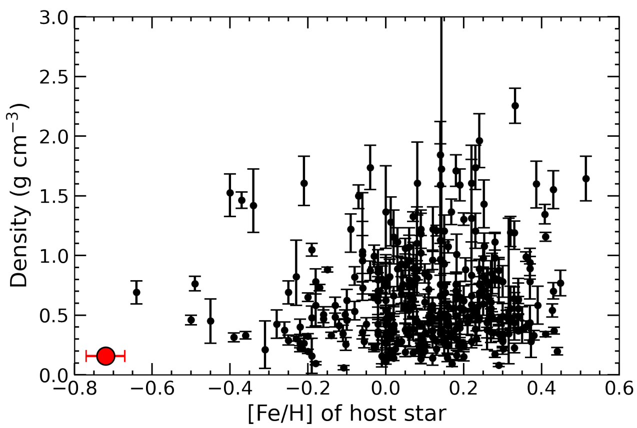

Figure 7. Giant planet densities as a function of host star metallicity. Data are taken from the TEPCat database (J. Southworth 2011). We plot planets with radii between 1 and 1.5 $R_{\rm Jup}$ and masses less than 2.0 $M_{\rm Jup}$. TOI-7169 b is displayed as a large red circle. Although it may appear by eye that the planets around the most metal-poor host stars are biased to lower densities, the large number of low density planets with metal-rich hosts that are obscured in the bulk of the distribution mean that this tendency is not statistically significant.

of TOI-7169 b are consistent with this trend extending to larger planets as well. However, WASP-37 b, WASP-46 b, and WASP-163 b represent counterexamples of giant planets with Jupiter-like densities despite host star metallicities of [Fe/H] < -0.3 (E. K. Simpson et al. 2011; S. Ciceri et al. 2016; K. Barkaoui et al. 2019). The full population of exoplanets with similar sizes from the database of J. Southworth (2011) shows no correlation of density with host star metallicity, and a K-S test indicates that the densities of giant planets around metal-poor host stars are consistent with being drawn from the same distribution as the densities of giant planets with metal-rich hosts (see Figure 7). Thus, TOI-7169 b may be inflated by the hot Jupiter radius anomaly rather than a metallicity-specific mechanism, although models do suggest that a lower bulk metallicity results in larger radii (Y. Chachan et al. 2025).

5.3. Orbit in the Milky Way

Using the distance, proper motion, and velocity of TOI-7169 from Gaia DR3, we computed the orbit of the star around the Galaxy with the `gala` package (A. M. Price-Whelan 2017). The orbital path over the last 1 Gyr is displayed in Figure 8. The orbit is confined within the Milky Way disk, with a moderate eccentricity of $e = 0.24$. The pericenter of the orbit is 5.8 kpc and the apocenter is 9.4 kpc, so TOI-7169 remains within ∼2 kpc of the solar circle throughout its orbit. Surprisingly for such an old star, the orbit is confined within 200 pc of the Galactic plane. TOI-7169 was likely born close to the time that the Milky Way disk first formed (e.g., V. Belokurov & A. Kravtsov 2022).

There are innumerable analyses of the structure of the Milky Way disk in the literature, which reach different quantitative conclusions about the scale heights of the thin and thick disks based on the stellar tracer used, the age and metallicity (and [α/Fe]) ranges considered, and the parameterization adopted for the structure of each component. However, broadly speaking, the thin disk scale height is generally found to be $\lesssim$300 pc (e.g., J. Bland-Hawthorn & O. Gerhard 2016) whereas the thick disk scale height is $\gtrsim$500 pc (e.g., A. C. Robin et al. 2014; J. Bland-Hawthorn & O. Gerhard 2016). For old and α-enhanced stars, the scale height locally is again at least ∼500 pc (e.g., J. T. Mackereth et al. 2017; C. Mateu & A. K. Vivas 2018; J. Imig et al. 2025; M. Xiang et al. 2025). The median absolute deviation of the TOI-7169 orbit from the Galactic midplane of 127 pc is therefore more consistent with the thin disk. Using Gaia DR3 kinematics, the U, V, and W space velocities of TOI-7169 are -67.70, -39.00, and -1.49 km s^{-1}, respectively. The U and V velocities and the total space velocity ($\sqrt{U^2 + V^2 + W^2} = 78.1$ km s^{-1}) are consistent with the thick disk (see Figure 9), but as noted above, the behavior in the z-direction is much more characteristic of the thin disk. Using the method of T. Bensby et al. (2014), the ratio of the thick disk membership probability to that of the thin disk is 0.11.

5.4. Spectroscopy Metrics

Many of the atoms and molecules found in giant planet atmospheres are composed of metals (e.g., H. R. Wakeford & D. K. Sing 2015; A. Dyrek et al. 2024; H. J. Hoeijmakers et al. 2024; A. Gressier et al. 2025; D. R. Louie et al. 2025; S. Saha & J. S. Jenkins 2025). It is likely that the abundance of these species and the overall atmospheric chemistry are affected by the availability of metals during planet formation. TOI-7169 b may therefore represent an intriguing contrast with the hot Jupiters around primarily metal-rich host stars that have been studied recently with JWST and other telescopes. In the framework of E. M.-R. Kempton et al. (2018), we compute a transmission spectroscopy metric (TSM) of 166, making the planet a quite feasible target for spectroscopy with JWST. Objects with similar TSM values that have already been studied with JWST include GJ 9827 d (C. Piaulet-Ghorayeb et al. 2024), LTT 9779 b (M. Radica et al. 2024), and Kepler-51 d (J. E. Libby-Roberts et al. 2026). The emission spectroscopy metric of TOI-7169 b of 54 is somewhat less favorable, but still in the range of other JWST targets whose emission spectra have been detected (e.g., WASP-17 b: A. Gressier et al. 2025; 55 Cnc e: R. Hu et al. 2024; J. A. Patel et al. 2024).

5.5. Implications for Hot Jupiter Formation and Evolution

Theoretical models suggest that planet formation may be inhibited below a critical metallicity. The small number of known planets in the metal-poor regime, however, has made it difficult to test this idea quantitatively. Based on the timescale for dust grain settling in a protoplanetary disk, J. L. Johnson & H. Li (2012) found a minimum metallicity of $[\mathrm{Fe/H}]_{\mathrm{crit}} \simeq -1.5 + \log(r/1\ \mathrm{au})$. At the current semimajor axis of 0.04 au for TOI-7169 b, this limit translates to [Fe/H] $= -2.9$, which is far below the actual metallicity of TOI-7169. Plugging the measured metallicity into this framework, the planet would need to have formed at a distance of no more than 6 au from the host star. If the system contains additional planets at longer periods (see below), the formation scenario constraints may become stronger.

With an age of 12 Gyr, TOI-7169 b is one of the oldest known planets (e.g., T. L. Campante et al. 2015; N. Grieves et al. 2022; A. Weeks et al. 2025). Since various formation pathways for hot Jupiters have been proposed, the properties of this system may provide insight into the formation of other hot Jupiters. One interesting question that may be investigated with future observations is whether TOI-7169 hosts an outer

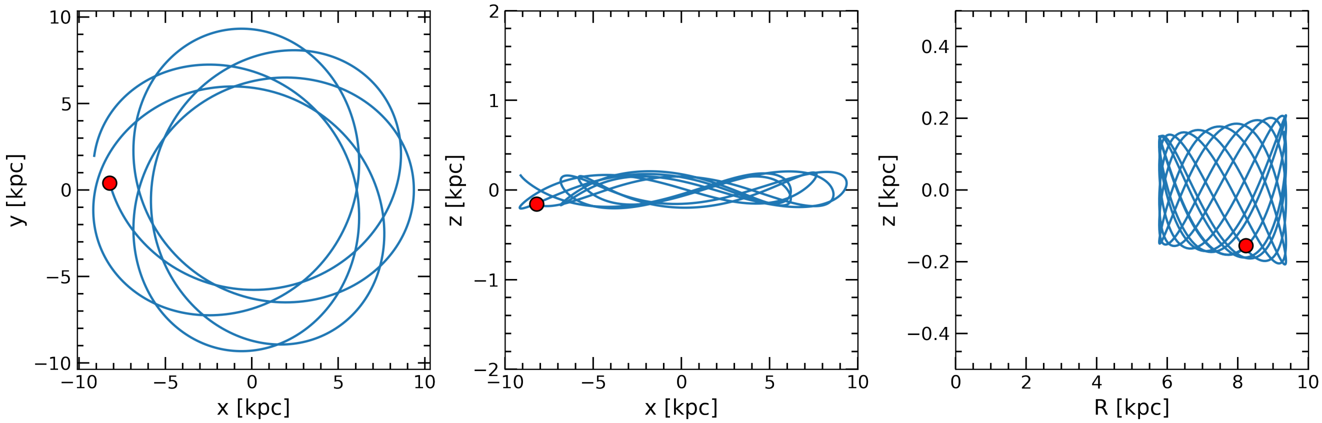

Figure 8. Galactic orbit of TOI-7169 over the past 1 Gyr. The left panel shows the orbit in the Cartesian *x*–*y* plane, the middle panel in the Cartesian *x*–*z* plane, and the right panel in cylindrical coordinates. Note the change in *y*-axis scale between the middle and right panels. In each panel, the red circle indicates the current position of TOI-7169. As expected for an old star, the orbit is somewhat eccentric, but it remains confined within a narrow range around the Galactic plane.

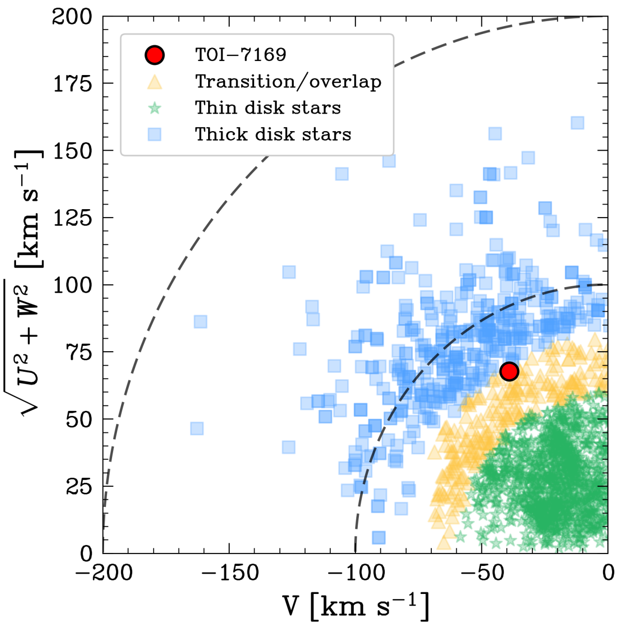

Figure 9. Toomre diagram for TOI-7169. The dashed curves indicate constant total velocities of 100 and 200 km s^{-1}. Green stars, yellow triangles, and blue squares represent the thin disk ($v_{tot} \leqslant 60$ km s^{-1}), transition/overlap ($60 < v_{tot} \leqslant 80$ km s^{-1}), and thick disk ($80 < v_{tot} \leqslant 180$ km s^{-1}) populations, respectively, following the definitions of S. Feltzing et al. (2003). Data taken from the NASA Exoplanet Archive (R. L. Akeson et al. 2013).

companion that could have been responsible for high-eccentricity migration of TOI-7169 b (e.g., R. I. Dawson & J. A. Johnson 2018). The lack of an RV signal with an amplitude above ∼200 m s^{-1} over the 9 yr covered by our spectroscopy rules out stellar or brown dwarf companions with periods less than 1–2 decades. Wider companions in the G and K star range should also have been detected in our existing data, but a low-mass M dwarf or brown dwarf in a long-period orbit could have escaped detection. At shorter periods (∼1–10 yr), additional giant planets cannot be excluded without an improved RV dataset. Long-term RV monitoring, higher contrast imaging, and searches for transiting objects with longer periods could detect or further constrain the existence of such a companion. Astrometric measurements from the fourth Gaia data release could also be sensitive to a companion, although the RUWE and astrometric excess noise in DR3 do not currently provide any evidence that the motion of TOI-7169 deviates from that of a single star.

6. Conclusions

As part of a program aiming to find transiting planets around metal-poor stars, we have presented the discovery and characterization of the giant planet TOI-7169 b. TOI-7169 was identified as exhibiting the signal of a potential transiting planet by the TESS team. We selected it from the list of TOIs as a candidate metal-poor planet host based on metallicity estimates from Gaia spectrophotometry.

We obtained ground-based imaging and spectroscopy of TOI-7169 that confirmed both the existence of the planet TOI-7169 b and the metal-poor nature of the host star. TOI-7169 is a slightly evolved early G star with a mass of $0.885 \pm 0.010\,M_{\odot}$, a metallicity of $[Fe/H] = -0.72 \pm 0.05$, and an age of 12.3 ± 0.6 Gyr. Based on this metallicity measurement, TOI-7169 is the most metal-poor star known to host a transiting giant planet. The star is α enhanced, at $[\alpha/Fe] = 0.29$, but despite its old age and low metallicity, its Galactic orbit identifies it as a member of the thin disk population, reaching a maximum distance from the Galactic plane of 200 pc.

We determined that TOI-7169 b is a giant planet with a radius of $1.475 \pm 0.029\,R_{Jup}$, a mass of $0.41 \pm 0.14\,M_{Jup}$, and an orbital period of 3.44 days. The planetary density is quite low ($0.159^{+0.055}_{-0.054}$ g cm^{-3}) and its orbit is consistent with being circular. The available data do not provide any evidence of a longer-period companion in the system that could be responsible for the migration of TOI-7169 b to its current location, but we cannot rule out additional planets at the Jupiter or super-Jupiter mass scale in orbits beyond ∼1 au.

The unique combination of the large radius of the planet, the low metallicity of the host star, and its relatively bright magnitude ($J = 11.20$) make TOI-7169 a promising target for transmission spectroscopy. Comparison of the atmospheric structure and composition with those of other planets orbiting more metal-rich stars may provide insight into how planetary atmospheres are affected by the availability of heavy elements. Moreover, the survival of TOI-7169 b for more than 12 Gyr will constrain the evolutionary processes that shape planets over long timescales.

Acknowledgments

We thank Allyson Bieryla, Madeleine McKenzie, Emily Pass, and Shreyas Vissapragada for advice and assistance during this work. We thank the anonymous referee for suggestions that clarified the paper.

This research has made use of NASA's Astrophysics Data System Bibliographic Services.

Funding for the TESS mission is provided by NASA's Science Mission Directorate.

This research has made use of the Exoplanet Follow-up Observation Program (ExoFOP)[40] website, which is operated by the California Institute of Technology, under contract with the National Aeronautics and Space Administration under the Exoplanet Exploration Program.

K.A.C. acknowledges support from the TESS mission via subaward s3449 from MIT. A.C. is supported by the Brinson Foundation through a Brinson Prize Fellowship grant. Funding for K.B. was provided by the European Union (ERC AdG SUBSTELLAR, GA 101054354). We acknowledge financial support from the Agencia Estatal de Investigación of the Ministerio de Ciencia e Innovación MCIN/AEI/10.13039/501100011033 and the ERDF "A way of making Europe" through projects PID2021-125627OB-C32 and PID2024-158486OB-C32. F.M. acknowledges the financial support from the Agencia Estatal de Investigación del Ministerio de Ciencia, Innovación y Universidades (MCIU/AEI) through grant PID2023-152906NA-I00. This work was partly supported by JSPS KAKENHI grant Nos. JP24H00017 and JP24K00689 and JSPS Bilateral Program Number JPJSBP120249910.

This paper has made use of the Python package GaiaXPy, developed and maintained by members of the Gaia Data Processing and Analysis Consortium (DPAC), and in particular, Coordination Unit 5 (CU5), and the Data Processing Centre located at the Institute of Astronomy, Cambridge, UK (DPCI).

This article is based on observations made with the MuSCAT2 instrument, developed by ABC, at Telescopio Carlos Sánchez operated on the island of Tenerife by the IAC in the Spanish Observatorio del Teide.

Some of the observations in this paper made use of the NN-EXPLORE Exoplanet and Stellar Speckle Imager (NESSI). NESSI was funded by the NASA Exoplanet Exploration Program and the NASA Ames Research Center. NESSI was built at the Ames Research Center by S.B.H., Nic Scott, Elliott P. Horch, and Emmett Quigley.

This work makes use of observations from the LCOGT network. Part of the LCOGT telescope time was granted by NOIRLab through the Mid-Scale Innovations Program (MSIP). MSIP is funded by NSF.

TRAPPIST is funded by the Belgian Fund for Scientific Research (Fond National de la Recherche Scientifique, FNRS) under the grant PDR T.0120.21. TRAPPIST-North is a project funded by the University of Liege (Belgium), in collaboration with Cadi Ayyad University of Marrakech (Morocco). M.G. and E.J. are FNRS-F.R.S. Research Directors.

Facilities: TESS, Gaia, FLWO:1.5 m, TRAPPIST, LCOGT, MuSCAT2.

Software: AstroImageJ (K. A. Collins et al. 2017), astropy (Astropy Collaboration et al. 2018), EXOFASTv2 (J. Eastman et al. 2013; J. D. Eastman et al. 2019), gala (A. M. Price-Whelan 2017), IRAF, keplersplinev2 (A. Vanderburg & J. A. Johnson 2014), kmpfit (J. P. Terlouw & M. G. R. Vogelaar 2015), lightkurve (Lightkurve Collaboration et al. 2018), matplotlib (J. D. Hunter 2007), MOOG (C. A. Sneden 1973), Qoyllur-quipu (I. Ramírez et al. 2014), TAPIR (E. Jensen 2013), uberMS (E. K. Pass et al. 2025).

[40] DOI: 10.26134/ExoFOP5

ORCID iDs

Joshua D. Simon https://orcid.org/0000-0002-4733-4994
Joseph E. Rodriguez https://orcid.org/0000-0001-8812-0565
Jhon Yana Galarza https://orcid.org/0000-0001-9261-8366
David W. Latham https://orcid.org/0000-0001-9911-7388
Victoria DiTomasso https://orcid.org/0000-0003-0741-7661
Karen A. Collins https://orcid.org/0000-0001-6588-9574
Jack Schulte https://orcid.org/0000-0002-7382-0160
Anirudh Chiti https://orcid.org/0000-0002-7155-679X
Samuel N. Quinn https://orcid.org/0000-0002-8964-8377
Mohammad K. Mardini https://orcid.org/0000-0001-9178-3992
Shubham Kanodia https://orcid.org/0000-0001-8401-4300
Johanna K. Teske https://orcid.org/0009-0008-2801-5040
Peter S. Ferguson https://orcid.org/0000-0001-6957-1627
Samuel W. Yee https://orcid.org/0000-0001-7961-3907
T. G. Tan https://orcid.org/0000-0001-5603-6895
Khalid Alsubai https://orcid.org/0000-0001-6253-0179
Khalid Barkaoui https://orcid.org/0000-0003-1464-9276
Zouhair Benkhaldoun https://orcid.org/0000-0001-6285-9847
Krzysztof Bernacki https://orcid.org/0000-0003-4647-7114
Jerome P. de Leon https://orcid.org/0000-0002-6424-3410
Sarah J. Deveny https://orcid.org/0009-0002-9833-0667
Mark E. Everett https://orcid.org/0000-0002-0885-7215
Izuru Fukuda https://orcid.org/0000-0002-9436-2891
Akihiko Fukui https://orcid.org/0000-0002-4909-5763
Michaël Gillon https://orcid.org/0000-0003-1462-7739
Arvind F. Gupta https://orcid.org/0000-0002-5463-9980
Steve B. Howell https://orcid.org/0000-0002-2532-2853
Emmanuel Jehin https://orcid.org/0000-0001-8923-488X
Gaia Lacedelli https://orcid.org/0000-0002-4197-7374
Adam Lark https://orcid.org/0009-0009-2881-7112
Colin Littlefield https://orcid.org/0000-0001-7746-5795
Felipe Murgas https://orcid.org/0000-0001-9087-1245
Norio Narita https://orcid.org/0000-0001-8511-2981
Enric Palle https://orcid.org/0000-0003-0987-1593
Hannu Parviainen https://orcid.org/0000-0001-5519-1391
Adam Popowicz https://orcid.org/0000-0003-3184-5228
Richard P. Schwarz https://orcid.org/0000-0001-8227-1020
Avi Shporer https://orcid.org/0000-0002-1836-3120
Abderahmane Soubkiou https://orcid.org/0000-0002-0345-2147
Francis P. Wilkin https://orcid.org/0000-0003-2127-8952

References

Adams Redai, J., Chandra, V., Yee, S. W., et al. 2026, ApJL, 1002, L41
Akeson, R. L., Chen, X., Ciardi, D., et al. 2013, PASP, 125, 989
Ali-Dib, M., Mousis, O., Petit, J.-M., & Lunine, J. I. 2014, ApJ, 785, 125

Amarsi, A. M., Asplund, M., Collet, R., & Leenaarts, J. 2015, MNRAS, 454, L11
Anderson, D. R., Brown, D. J. A., Collier Cameron, A., et al. 2014, arXiv:1410.3449
Anglada-Escude, G., Arriagada, P., Tuomi, M., et al. 2014, MNRAS, 443, L89
Asplund, M., Amarsi, A. M., & Grevesse, N. 2021, A&A, 653, A141
Astropy Collaboration, Price-Whelan, A. M., Sipőcz, B. M., et al. 2018, AJ, 156, 123
Ballard, S. 2024, arXiv:2409.10485
Barbato, D., Sozzetti, A., Biazzo, K., et al. 2019, A&A, 621, A110
Barkaoui, K., Burdanov, A., Hellier, C., et al. 2019, AJ, 157, 43
Behmard, A., Brinkman, C. L., Hattori, S., Rubenzahl, R. A., & Bedell, M. 2025, AJ, 170, 282
Belokurov, V., & Kravtsov, A. 2022, MNRAS, 514, 689
Belokurov, V., Penoyre, Z., Oh, S., et al. 2020, MNRAS, 496, 1922
Bensby, T., Feltzing, S., & Oey, M. S. 2014, A&A, 562, A71
Blackwell-Whitehead, R. J., Pickering, J. C., Pearse, O., & Nave, G. 2005a, ApJS, 157, 402
Blackwell-Whitehead, R. J., Toner, A., Hibbert, A., Webb, J., & Ivarsson, S. 2005b, MNRAS, 364, 705
Bland-Hawthorn, J., & Gerhard, O. 2016, ARA&A, 54, 529
Boley, K. M., Wang, J., Zinn, J. C., et al. 2021, AJ, 162, 85
Boley, K. M., Christiansen, J. L., Zink, J., et al. 2024, AJ, 168, 128
Bortle, A., Fausey, H., Ji, J., et al. 2021, AJ, 161, 230
Brewer, J. M., Wang, S., Fischer, D. A., & Foreman-Mackey, D. 2018, ApJL, 867, L3
Brown, T. M., Baliber, N., Bianco, F. B., et al. 2013, PASP, 125, 1031
Brown, T. M., Tumlinson, J., Geha, M., et al. 2014, ApJ, 796, 91
Buchhave, L. A., Bakos, G. Á., Hartman, J. D., et al. 2010, ApJ, 720, 1118
Buchhave, L. A., Latham, D. W., Johansen, A., et al. 2012, Natur, 486, 375
Buder, S., Kos, J., Wang, X. E., et al. 2025, PASA, 42, e051
Caldwell, D. A., Tenenbaum, P., Twicken, J. D., et al. 2020, RNAAS, 4, 201
Campante, T. L., Barclay, T., Swift, J. J., et al. 2015, ApJ, 799, 170
Castelli, F., & Kurucz, R. L. 2003, IAUS, 210, A20
Chachan, Y., Fortney, J. J., Ohno, K., Thorngren, D., & Murray-Clay, R. 2025, ApJ, 994, 43
Chiti, A., Frebel, A., Jerjen, H., Kim, D., & Norris, J. E. 2020, ApJ, 891, 8
Chiti, A., Frebel, A., Mardini, M. K., et al. 2021, ApJS, 254, 31
Choi, J., Dotter, A., Conroy, C., et al. 2016, ApJ, 823, 102
Christiansen, J. L., McElroy, D. L., Harbut, M., et al. 2025, PSJ, 6, 186
Ciceri, S., Mancini, L., Southworth, J., et al. 2016, MNRAS, 456, 990
Cohen, J. G., Christlieb, N., Qian, Y. Z., & Wasserburg, G. J. 2003, ApJ, 588, 1082
Collins, K. 2019, AAS, 233, 140.05
Collins, K. A., Kielkopf, J. F., Stassun, K. G., & Hessman, F. V. 2017, AJ, 153, 77
Cutri, R. M., Skrutskie, M. F., van Dyk, S., et al. 2003, 2MASS All Sky Catalog of Point Sources (NASA)
Cutri, R. M., Wright, E. L., Conrow, T., et al. 2021, yCat, 2328, 0
Dawson, R. I., & Johnson, J. A. 2018, ARA&A, 56, 175
de Leon, J. P., Livingston, J., Endl, M., et al. 2021, MNRAS, 508, 195
Delgado Mena, E., Adibekyan, V., Santos, N. C., et al. 2021, A&A, 655, A99
Demarque, P., Woo, J.-H., Kim, Y.-C., & Yi, S. K. 2004, ApJS, 155, 667
DiTomasso, V., Charbonneau, D., Vanderburg, A., et al. 2025, arXiv:2508.16805
DiTomasso, V., Yee, S. W., Rodríguez Martínez, R., et al. 2026, AJ, in press
Dotter, A., Chaboyer, B., Jevremović, D., et al. 2008, ApJS, 178, 89
Dyrek, A., Min, M., Decin, L., et al. 2024, Natur, 625, 51
Eastman, J., Gaudi, B. S., & Agol, E. 2013, PASP, 125, 83
Eastman, J. D., Rodriguez, J. E., Agol, E., et al. 2019, arXiv:1907.09480
El-Badry, K., Rix, H.-W., & Heintz, T. M. 2021, MNRAS, 506, 2269
Fabricius, C., Luri, X., Arenou, F., et al. 2021, A&A, 649, A5
Faria, J. P., Santos, N. C., Figueira, P., et al. 2016, A&A, 589, A25
Feltzing, S., Bensby, T., & Lundström, I. 2003, A&A, 397, L1
Ferreira, T., Yana Galarza, J., Reggiani, H., et al. 2025, arXiv, arXiv:2512.17072
Fűrész, G. 2008, PhD thesis, Univ. Szeged, Hungary
Fischer, D. A., & Valenti, J. 2005, ApJ, 622, 1102
Gaia Collaboration, Prusti, T., de Bruijne, J., H., J., et al. 2016, A&A, 595, A1
Gaia Collaboration, Smart, R. L., Sarro, L. M., et al. 2021, A&A, 649, A6
Gaia Collaboration, Montegriffo, P., Bellazzini, M., et al. 2023a, A&A, 674, A33
Gaia Collaboration, Vallenari, A., Brown, A. G. A., et al. 2023b, A&A, 674, A1
Gaia Collaboration, Arenou, F., Babusiaux, C., et al. 2023c, A&A, 674, A34
GaiaXPy 2022, gaia-dpci/GaiaXPy: Release v1.0.0,
Green, G. M., Schlafly, E., Zucker, C., Speagle, J. S., & Finkbeiner, D. 2019, ApJ, 887, 93
Gressier, A., MacDonald, R. J., Espinoza, N., et al. 2025, AJ, 169, 57
Grieves, N., Bouchy, F., Ulmer-Moll, S., et al. 2022, A&A, 668, A29
Guerrero, N. M., Seager, S., Huang, C. X., et al. 2021, ApJS, 254, 39
Hallatt, T., & Lee, E. J. 2025, ApJ, 979, 120
Hellier, C., Anderson, D. R., Collier Cameron, A., et al. 2014, MNRAS, 440, 1982
Helling, C., Tootill, D., Woitke, P., & Lee, E. 2017, A&A, 603, A123
Hinkel, N. R., Timmes, F. X., Young, P. A., Pagano, M. D., & Turnbull, M. C. 2014, AJ, 148, 54
Hoeijmakers, H. J., Kitzmann, D., Morris, B. M., et al. 2024, A&A, 685, A139
Howell, S. B., Everett, M. E., Sherry, W., Horch, E., & Ciardi, D. R. 2011, AJ, 142, 19
Hu, R., Bello-Arufe, A., Zhang, M., et al. 2024, Natur, 630, 609
Huang, C. X., Vanderburg, A., Pál, A., et al. 2020a, RNAAS, 4, 204
Huang, C. X., Vanderburg, A., Pál, A., et al. 2020b, RNAAS, 4, 206
Hunter, J. D. 2007, CSE, 9, 90
Imig, J., Holtzman, J. A., Zasowski, G., et al. 2025, ApJ, 990, 203
Jenkins, J. M., Twicken, J. D., McCauliff, S., et al. 2016, SPIE, 9913, 99133E
Jensen, E. 2013, Tapir: A web interface for transit/eclipse observability, Astrophysics Source Code Library, ascl:1306.007
Johnson, J. L., & Li, H. 2012, ApJ, 751, 81
Keller, S. C., Schmidt, B. P., Bessell, M. S., et al. 2007, PASA, 24, 1
Kempton, E. M.-R., Bean, J. L., Louie, D. R., et al. 2018, PASP, 130, 114401
Klose, J. Z., Fuhr, J. R., & Wiese, W. L. 2002, JPCRD, 31, 217
Lawler, J. E., Wood, M. P., Den Hartog, E. A., et al. 2014, ApJS, 215, 20
Lee, B. C., Park, M. G., Lee, S. M., et al. 2015, A&A, 584, A79
Libby-Roberts, J. E., Bello-Arufe, A., Berta-Thompson, Z. K., et al. 2026, AJ, 171, 221
Lightkurve Collaboration, Cardoso, J. V. d. M., Hedges, C., et al. 2018, Lightkurve: Kepler and TESS time series analysis in Python, Astrophysics Source Code Library, ascl:1812.013
Lindegren, L., Klioner, S. A., Hernández, J., et al. 2021, A&A, 649, A2
Louie, D. R., Mullens, E., Alderson, L., et al. 2025, AJ, 169, 86
Mackereth, J. T., Bovy, J., Schiavon, R. P., et al. 2017, MNRAS, 471, 3057
Madhusudhan, N., Mousis, O., Johnson, T. V., & Lunine, J. I. 2011, ApJ, 743, 191
Mancini, L., Giordano, M., Mollière, P., et al. 2016, MNRAS, 461, 1053
Martin, N. F., Starkenburg, E., Yuan, Z., et al. 2024, A&A, 692, A115
Martos, G., Meléndez, J., Rathsam, A., & Carvalho Silva, G. 2023, MNRAS, 522, 3217
Mateu, C., & Vivas, A. K. 2018, MNRAS, 479, 211
McCully, C., Volgenau, N. H., Harbeck, D.-R., et al. 2018, SPIE, 10707, 107070K
McWilliam, A. 1998, AJ, 115, 1640
Meléndez, J., Ramírez, I., Karakas, A. I., et al. 2014, ApJ, 791, 14
Moe, M., Kratter, K. M., & Badenes, C. 2019, ApJ, 875, 61
Mortier, A., Santos, N. C., Sousa, S., et al. 2013, A&A, 551, A112
Mortier, A., Santos, N. C., Sozzetti, A., et al. 2012, A&A, 543, A45
Morton, T. D., Bryson, S. T., Coughlin, J. L., et al. 2016, ApJ, 822, 86
Narita, N., Fukui, A., Kusakabe, N., et al. 2019, JATIS, 5, 015001
Parviainen, H., Palle, E., Zapatero-Osorio, M. R., et al. 2020, A&A, 633, A28
Pass, E. K., Cargile, P. A., DiTomasso, V., et al. 2025, ApJS, 281, 27
Patel, J. A., Brandeker, A., Kitzmann, D., et al. 2024, A&A, 690, A159
Pavlenko, Y. V., Kaminsky, B. M., Jenkins, J. S., et al. 2019, A&A, 621, A112
Penoyre, Z., Belokurov, V., & Evans, N. W. 2022, MNRAS, 513, 2437
Petigura, E. A., Marcy, G. W., Winn, J. N., et al. 2018, AJ, 155, 89
Piaulet-Ghorayeb, C., Benneke, B., Radica, M., et al. 2024, ApJL, 974, L10
Price-Whelan, A. M. 2017, JOSS, 2, 388
Prochaska, J. X., & McWilliam, A. 2000, ApJL, 537, L57
Prochaska, J. X., Naumov, S. O., Carney, B. W., McWilliam, A., & Wolfe, A. M. 2000, AJ, 120, 2513
Quinn, S. N., White, R. J., Latham, D. W., et al. 2012, ApJL, 756, L33
Radica, M., Coulombe, L.-P., Taylor, J., et al. 2024, ApJL, 962, L20
Ramírez, I., Meléndez, J., Bean, J., et al. 2014, A&A, 572, A48
Ricker, G. R., Winn, J. N., Vanderspek, R., et al. 2015, JATIS, 1, 014003
Riello, M., De Angeli, F., Evans, D. W., et al. 2021, A&A, 649, A3
Robin, A. C., Reylé, C., Fliri, J., et al. 2014, A&A, 569, A13
Rodriguez, J. E., Quinn, S. N., Zhou, G., et al. 2021, AJ, 161, 194
Rodríguez Martínez, R., Martin, D. V., Gaudi, B. S., et al. 2023, AJ, 166, 137
Saha, S., & Jenkins, J. S. 2025, ApJL, 994, L39
Salaris, M., Chieffi, A., & Straniero, O. 1993, ApJ, 414, 580
Santos, N. C., Mayor, M., Bonfils, X., et al. 2011, A&A, 526, A112
Schlegel, D. J., Finkbeiner, D. P., & Davis, M. 1998, ApJ, 500, 525
Schulte, J., Rodriguez, J. E., Bieryla, A., et al. 2024, AJ, 168, 32

Schulte, J., Rodriguez, J. E., Latham, D. W., et al. 2025, MNRAS, 543, 292
Scott, N. J., Howell, S. B., Horch, E. P., & Everett, M. E. 2018, PASP, 130, 054502
Scott, N. J., Howell, S. B., Gnilka, C. L., et al. 2021, FrASS, 8, 138
Shejeelammal, J., Meléndez, J., Rathsam, A., & Martos, G. 2024, A&A, 690, A107
Simpson, E. K., Faedi, F., Barros, S. C. C., et al. 2011, AJ, 141, 8
Sneden, C. A. 1973, PhD thesis, The University of Texas at Austin
Southworth, J. 2011, MNRAS, 417, 2166
Sozzetti, A., Torres, G., Latham, D. W., et al. 2009, ApJ, 697, 544
Starkenburg, E., Martin, N., Youakim, K., et al. 2017, MNRAS, 471, 2587
Szentgyorgyi, A. H., & Furész, G. 2007, RMxAC, 28, 129
Takarada, T., Sato, B., Omiya, M., et al. 2018, PASJ, 70, 59
Terlouw, J. P., & Vogelaar, M. G. R. 2015, Kapteyn Package (Kapteyn Astronomical Institute)
Vanderburg, A., & Johnson, J. A. 2014, PASP, 126, 948
Villaver, E., Niedzielski, A., Wolszczan, A., et al. 2017, A&A, 606, A38
Vissapragada, S., & Behmard, A. 2025, AJ, 169, 117
Wakeford, H. R., & Sing, D. K. 2015, A&A, 573, A122
Weeks, A., Huber, D., Stokholm, A., et al. 2025, MNRAS, 541, 2459
Winter, A. J., Benisty, M., & Andrews, S. M. 2024, ApJL, 972, L9
Wright, E. L., Eisenhardt, P. R. M., Mainzer, A. K., et al. 2010, AJ, 140, 1868
Xiang, M., & Rix, H.-W. 2022, Natur, 603, 599
Xiang, M., Rix, H.-W., Yang, H., et al. 2025, NatAs, 9, 101
Yana Galarza, J., López-Valdivia, R., Meléndez, J., & Lorenzo-Oliveira, D. 2021a, ApJ, 922, 129
Yana Galarza, J., López-Valdivia, R., Lorenzo-Oliveira, D., et al. 2021b, MNRAS, 504, 1873
Yana Galarza, J., Reggiani, H., Ferreira, T., et al. 2024, ApJ, 974, 122
Yi, S., Demarque, P., Kim, Y.-C., et al. 2001, ApJS, 136, 417
Zink, J. K., Hardegree-Ullman, K. K., Christiansen, J. L., et al. 2023, AJ, 165, 262